

Time-resolved (kHz) 3D imaging of OH PLIF in a flame

Rikard Wellander · Mattias Richter ·
Marcus Aldén

Received: 20 November 2013 / Revised: 2 June 2014 / Accepted: 2 June 2014 / Published online: 14 June 2014
© Springer-Verlag Berlin Heidelberg 2014

Abstract Based on scanning planar laser-induced fluorescence of OH, a measurement system with the capability to record time-resolved three-dimensional image sequences of the OH concentration and the flame front is demonstrated on a premixed flame. A dual-mirror scanning system is used to obtain equidistance between the illuminated planes. Non-uniformities in the laser sheet and laser absorption in the flame are compensated for as the position- and time-dependent OH concentration is calculated throughout the measurement volume. A method for identifying the flame front in large data sets with a single set of filtering parameter is demonstrated. The artefacts introduced by the non-instantaneous recording of the measurement volume are suppressed using linear interpolation from successive recordings in the same measurement plane. The impact from filtering and image post-processing on the achieved spatial resolution is investigated. A final spatial and temporal resolution of $3.2 \times 3.2 \times 0.75$ lines/mm and 2 ms, respectively, are obtained in a measurement volume spanning $11 \times 22 \times 6$ mm during a time span of 0.5 s.

1 Introduction

Planar laser-induced fluorescence (PLIF) has been used for measurements of minor species concentration and

temperatures in combustion systems for many decades (Dyer and Crosley 1982). When conducted with an ordinary 10-Hz laser system, PLIF measurements provide snapshots of data from a cross-section of the flame that can be used for statistical analysis. However, ambiguities often arise due to the missing spatial dimension. What appears as a local quenching of the flame may as well be a bridging through the out-of-plane unrecorded space.

A common approach to extend the PLIF technique to the third spatial dimension is to rapidly scan the laser sheet through the measurement volume. Such an approach can be pursued with a high-repetition-rate laser (Yip et al. 1987; Kychakoff et al. 1987) in combination with a framing camera or through multiple exposures of a long laser pulse (Yip et al. 1988). When higher laser fluence is required, laser clusters can provide a short burst of high-power laser pulses. However, the approach is limited to rather few images, up to eight frames have been recorded for one 3D image in this manner (Hult et al. 2002; Olofsson et al. 2006; Nygren et al. 2002). The recent development of high-repetition-rate pulse burst mode lasers can provide more images during a similar short time period ~ 100 μ s (Thurrow and Lynch 2009; Thurrow et al. 2013). Other PLIF 3D approaches that do not utilize a scanning laser sheet are the crossed- and parallel-plane LIF from where semi-3D information can be extracted along a line or in a plane (Karpets et al. 2004; Oyoung and Bilger 1997). An optional approach where the laser is excluded consists of tomographic mapping of the chemiluminescence (Cai et al. 2013).

In addition to the third spatial dimension, the temporal dimension is also important, especially when it comes to study the flame dynamics. The early high-repetition-rate 2D PLIF studies rely on eximer (Kychakoff et al. 1987), copper vapor (Winter et al. 1987) or clustered Nd:YAG

Electronic supplementary material The online version of this article (doi:10.1007/s00348-014-1764-y) contains supplementary material, which is available to authorized users.

R. Wellander (✉) · M. Richter · M. Aldén
Division of Combustion Physics, Department of Physics,
Lund University, Box 118, 22100 Lund, Sweden
e-mail: rikard.wellander@forbrf.lth.se

lasers (Kaminski et al. 1999) in combination with framing cameras. More recent studies often rely on CMOS cameras in combination with solid-state diode-pumped Nd:YAG lasers for long image sequences (Smith and Sick 2005), or pulse burst mode systems for shorter images sequences, albeit with higher pulse fluence (Thurow et al. 2013).

Time-resolved 3D measurements would provide means to reveal the dynamics in complex flame geometries. Also, if combined with time-resolved 3D data of the flow field, it could be used to study flame flow interactions extensively. Such measurements would also provide information on the position- and time-dependent 3D flame front velocity, which is an important quantity in many reduced models of turbulent combustion (Trunk et al. 2013). However, time-resolved 3D measurements of laser-induced fluorescence have not before been realized.

Time-resolved 3D or quasi-3D recording of reacting flows can be achieved by means of chemiluminescence tomography, parallel- and crossed-plane PLIF (Trunk et al. 2013; Steinberg et al. 2011), and rapidly scanning PLIF. Chemiluminescence tomography is limited in repetition rate by the long exposure time required to obtain decent signal to noise ratio. Also, even though no laser system is needed, the amount of cameras that is required to achieve good accuracy will make the experiment expensive. The crossed- and parallel-plane PLIF have the advantage of high spatial and temporal resolution, but limit the record 3D data to a line and a plane, respectively. Scanning PLIF has the benefit of providing full 3D measurements with high in-plane resolution, but struggles with drawbacks such as reduced signal collection ability due to the required depth of field and artifacts that arise due to the non-instantaneous nature of the recording.

Here, a high-repetition-rate pulsed laser source is combined with scanning mirrors to demonstrate how

temporally resolved 3D information of the OH radical can be recorded. Numerous studies with the aim to quantify the OH concentration have been reported (Hertz and Alden 1987; Versluis et al. 1997; Arnold et al. 1997). Also, since it is formed early in the reaction and lives on in the product zone, it is commonly used as a marker for the flame front in premixed turbulent combustion (Hartung et al. 2008). A suitable methane/air flame is chosen as target for the demonstration and both flame front position and OH concentration is calculated from the recorded data. Challenges associated with this measurement technique, such as the control of the laser sheets depth positions, the non-instantaneous recording of each 3D image and the 3D interpretation of the recorded data, are addressed.

2 Scanning, laser and detection setup

The laser system consists of a frequency-doubled solid-state diode-pumped Nd:YAG laser (Edgewave HD40I-E), which in turn pump a dye laser (Sirah Credo). As seen in the experimental setup (Fig. 1), planar laser sheets for cross-sectional excitation of OH are obtained using ordinary sheet forming anti-reflective-coated UV optics. The depth dimension is resolved by scanning the laser sheet position back-and-forth through the flame. The maximum repetition rate of the pump laser is 20 kHz. Here, it is the scanning system, operated at 960 Hz, that triggers and thereby controls the exact repetition rate of the laser to 19.2 kHz. Thus, during one period of the scanning (back-and-forth), twenty laser shots are fired and data for two 3D images are recorded. An image intensifier (Lambert HS IRO 2 stage) in combination with a high-speed CMOS camera (Photron Fastcam SA-X) is synchronized to the laser system and used for detection of the OH fluorescence.

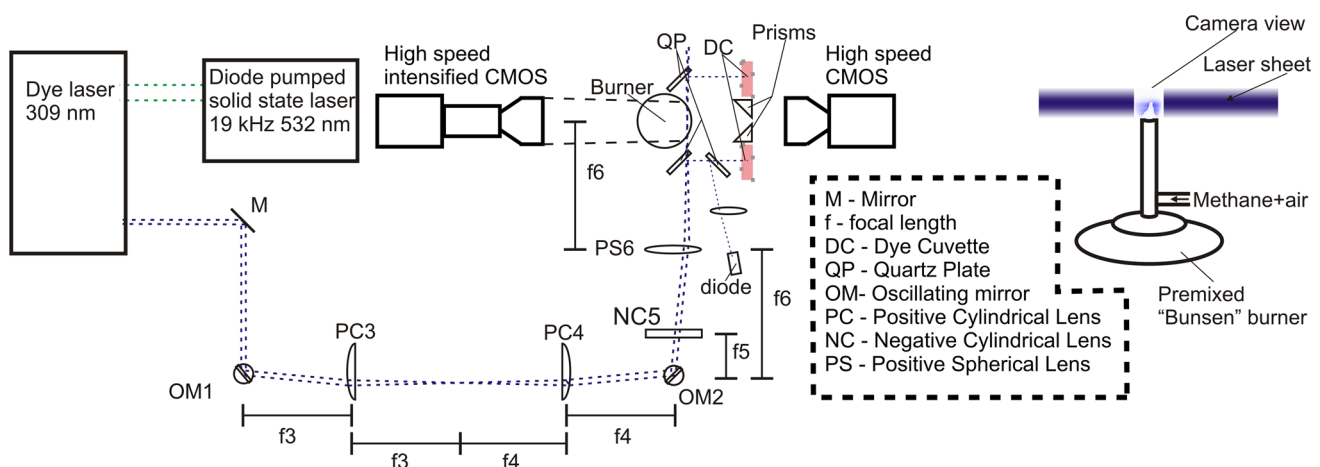


Fig. 1 *Left* Optical arrangement for time-resolved 3D OH measurements. *Right* schematic picture of the Bunsen burner. The air intake is sealed to allow for premixed fuel air mixtures of predefined stoichiometry

In order to avoid interference from scattered laser light, most OH fluorescence detection schemes target the A–X (1–0) vibrational band at 283 nm for excitation and the redshifted A–X (0–0) transition for detection. Here, the $Q_1(7)$ line of the A–X (0–0) transition at 309 nm is instead used for excitation. The four times higher absorption cross-section for this transition increases the precision in the absorption measurements that are used here to quantify the OH signal (Luque and Crosley 1998). In addition, it compensates for the reduction in obtainable laser fluency with Rhodamine B + Rhodamine 101 at 309 nm, which is about a third compared to what can be attained at 283 nm with Rhodamine 6G for the operation condition adopted here. Despite the low pulse energy ($10 \pm 5 \mu\text{J}$), signal to noise ratios (SNR) up to 30 ± 15 are achieved. Since the fluorescence spectrally overlaps the laser light, any light scattered toward the camera cannot be filtered away. Thus, for simultaneous measurements of the OH fluorescence and the flow field, by means of particle image velocimetry, or if the flame is confined by scattering surfaces, the A–X (1–0) would be a better target for excitation. The burner is a premixed Bunsen burner with sealed air intake, operated at an air/fuel ratio of $\lambda = 1.2$. The gas is first forced through a $\sim 0.4\text{-mm}$ hole in the bottom of the 1-cm-wide tube (8 cm upstream the flame), inducing a turbulent flow ($Re = 15,000$). However, at the flame, most of the turbulence has dissipated, creating the undulating flow as can be seen in the result section.

Since both the pump and the dye laser are operated close to their lasing thresholds, the output does not only fluctuate in terms of pulse energy. In addition, the spatial energy profile also varies from shot to shot. The standard deviation in the normalized energy profile is 11 %. Thus, it is essential that the energy profile is measured on a shot-to-shot basis. In addition to the energy fluctuations, the irradiance is also attenuated as the laser sheet propagates through the flame. To enable compensation for the attenuation and for fluctuations in the spatial energy profile of the laser light and calculation of the absorption coefficient, the laser fluence is measured both before and after the flame. These measurements are realized indirectly, by inserting two quartz plates in the beam path, reflecting portions of the laser sheet right before and after the flame into dye cuvettes. The induced fluorescence in the dye is recorded by a separate high-speed camera (Photron Fastcam SA5) according to Fig. 1. The dye solution is circulated through the cuvettes to avoid problems with bleaching and convection. A diode (Hamamatsu s1226 5BQ) records the pulse energy to enable correction for the difference in sensitivity in the fluence measurements as the laser sheets excite the dye in different regions of the dye cuvette during one scan.

If only one 3D image is recorded as in (Thurrow and Lynch 2009), the central linear part of the nonlinear mirror

scan may be utilized. However, if the flame is also resolved in time and the laser is operated at a constant repetition rate, the entire amplitude of the scan must be used unless some laser pulses are discarded. To achieve the same distance between the recorded planes, it is therefore important that the scanning is linear, i.e., follow a triangular pattern. This is achieved with two mirrors oscillating close to their eigenfrequency. One mirror works as a master for the triggering of the pump laser, the detection system and the second mirror. The second mirror is operated at the first odd overtone of the first mirror. As the sinusoidal deflections from the two mirrors are added together in a 4f system, the total deflection becomes more triangular shaped as opposed to the sinusoidal deflection obtained from a single oscillator. As a result, the laser sheets become more equidistant and larger scanning amplitude can be achieved with maintained spatial depth resolution. The laser sheet position in the flame is measured prior the ignition of the flame by imaging the back side of a thin diffusor, located at the center of the burner nozzle perpendicular to the laser sheet propagation, onto a high-speed camera (Photron SA5). The measured laser sheets positions are given in Fig. 2. It can here be seen that the phasing of the laser pulse sequence in relation to the mirror oscillation has been adjusted so that the sheet positions are the same regardless of sweep direction. Thus, two 3D images instead of one are recorded each period, increasing the time resolution at the cost of spatial resolution.

Due to difficulties in achieving a perfect phase shift between the two mirror oscillators, the positions of the laser sheets during the forward and backward sweep direction are not identical. This is the main limiting factor to the accuracy in the laser sheet positions and induces an

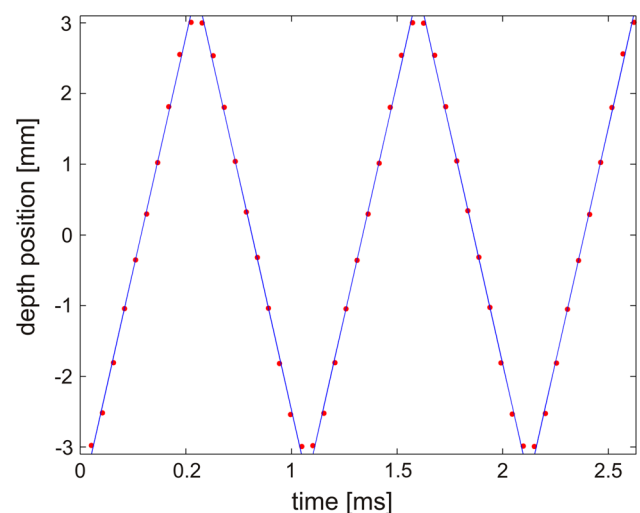


Fig. 2 Measured depth position of the laser sheet in the flame. Lines indicate a perfect triangular-shaped movement. The timing is adjusted for the laser sheet positions to overlap in the two sweep directions

error in the overlap of 6–49 μm depending on measurement plane. The accuracy could be improved by not assuming that the laser sheet positions are independent on sweep direction, and rather use the individually measured positions. It would then instead be limited by the achievable accuracy in the measurement of the laser sheet position. However, the accuracy is here considered to be adequate with respect to the inter sheet distance of 700 μm and to the laser sheet thickness of $2\omega_0 = 170 \mu\text{m}$ (measured with the knife edge method where ω_0 corresponds to the $1/e^2$ radius). Thus, the sheet positions are treated as being equal regardless of sweep direction. The precision in the laser sheet position is mainly limited by the time jitter in the triggering of the laser by the master oscillator. With the current settings, the standard deviation in the position of the laser sheets is 12 μm .

When interpreting the recorded OH signal, it is important to know whether it has a linear dependence to the laser irradiance, i.e., if the excitation is within the linear regime. With a quenching rate coefficient $Q_{21} \approx 5 \times 10^8 \text{s}^{-1}$ estimated from Jonsson et al. (2013) and transition probabilities from Luque and Crosley (1998), the saturation irradiance, I_{sat}^v , defined as in Eckbreth (1996) can be estimated to

$$I_{\text{sat}}^v = \frac{(A_{21} + Q_{21})c}{B_{21} + B_{12}} \approx 2.4 \times 10^6 \text{ Wcm}^{-2} \text{ Hz}^{-1} \quad (1)$$

where A_{21} , B_{21} and B_{12} are the rate constants for spontaneous emission, absorption and stimulated emission, respectively. With a spectral irradiance not exceeding $I_v = 6 \times 10^3 \text{ Wcm}^{-2} \text{ Hz}^{-1}$, the excitation is well within the linear regime. A separate measurement where the dye and diode response were related to a calibrated power meter (Thorlab 8322C) was performed to ensure that also the dye and diode provide a linear response.

Due to differences in the optics in front of the two cameras and in the different beam paths, the recordings of the OH signal and the laser sheet profiles before and after the flame may be shifted in relation to each other, both in terms of magnification and position. To enable compensation of these shifts, a transparent grating is temporarily inserted in the beam path, inducing a vertical intensity modulation in the laser sheet, as seen in Fig. 3. Twenty lines are identified in the different images providing data for accurate overlap between the recordings, both in terms of offset and magnification.

3 Temporal and spatial resolution

With one 3D image recorded every $\sim 0.5 \text{ ms}$, it can, according to the sampling theorem (Shannon 1949), be argued that fluctuations as short as 1 ms can be resolved.

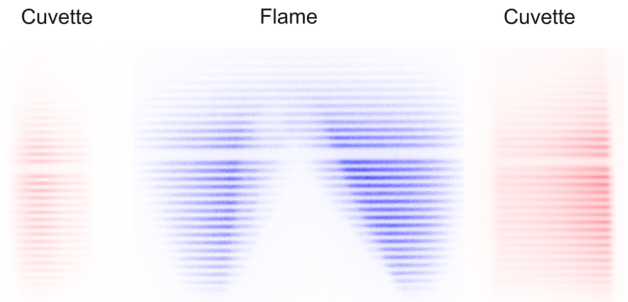


Fig. 3 Average recorded signal from the central cross-section as a spatial modulation is introduced into the laser sheet. *Left* initial dye cell. *Center* OH fluorescence. *Right* Final dye cell. The data are used to find a proper transformation function between the dye cells and the recording of the OH fluorescence. A slight difference in dye concentration causes the difference in intensity between the dye cells

However, the actual recordings in one 3D image are not instantaneous. The time difference between two overlapping planes ranges between 50 μs and 1 ms. Thus, the time resolution depends on depth position and varies from 1 ms in the center to 2 ms in the outer planes (see Fig. 2).

The spatial resolution obtained is influenced by several parameters. The in-plane spatial resolution is estimated to the highest spatial frequency that is resolved in the recording of a NBS 1963 resolution target as it is translated through the different laser sheet positions. It is mainly governed by the depth of field, the MCP gain voltage in the image intensifier and the filtering applied on the data. The aperture stop of the objective lens (Nikkor UV 105 mm) is set to match the depth of field to the scanning range. With a MCP voltage of the image intensifier set to 750 V, a constant resolution of $>5.6 \text{ lines/mm}$ for all image planes is reached with the aperture stop set to $f/8$. After low-pass filtering and prior calculation of the absorption coefficient, the resolution is reduced to 3.2 lines/mm. The filter size is 40×40 pixels and has a standard deviation of 3 pixels, corresponding to $1.1 \times 1.1 \text{ mm}^2$ and 86 μm , respectively. The calculation of the absorption coefficient should only have a minor effect on the resolution since the laser sheet spatial profile is obtained without an image intensifier at a higher resolution than the OH signal. When the nonlinear diffusion filter is applied to the image of the resolution target, no reduction of the resolution is seen. Thus, the final in-plane resolution is estimated to 3.2 lines/mm. One should bear in mind, however, that the nonlinear diffusion filtering depends on the data that are filtered, and it is therefore ambiguous to estimate the final resolution in the image of the OH flame front from the filtered image of the resolution target.

The depth resolution is governed by the thickness of, and distance between the laser sheets. Since the laser sheets are thinner (measured to 170 μm) than the spacing in between (700 μm), it is the inter sheet spacing that limits

the depth resolution. From the sampling theorem, this yields a spatial depth resolution of 0.75 lines/mm. This can be compared with the length scales present in the flame. The length scales are estimated from the 2D PLIF data originating from the central cross-section in the flame. Here, the direction of the gradients in the image is calculated as

$$\hat{n} = \arctan\left(\frac{\partial S_f / \partial y}{\partial S_f / \partial x}\right) \quad (2)$$

where $\partial S_f / \partial y$ and $\partial S_f / \partial x$ correspond to the vertical and horizontal gradients in the signal, respectively. The direction of the gradients in the position of the calculated flame front is stored in a vector $\hat{n}(l)$, where l represents the distance along the flame front. The derivative of this vector, i.e., the change of direction of the flame front, represents the curvature, κ , in the plane

$$\kappa = \frac{\partial \hat{n}(l)}{\partial l} \quad (3)$$

The resolvable scales can be estimated from the diameter of a circle with the same curvature as the flame front. Figure 4 shows a histogram of the length scales from the central cross-section, calculated in this manner. It can here be seen that the smallest length scales remain unresolved with the current depth resolution, although the majority of the scales in the histogram are resolved.

Another feature that may influence the spatial resolution is beam steering induced by the thermal gradients in the flame. The magnitude of the beam steering can be derived from measurements where the vertical intensity modulation is imposed on the laser sheet (see Fig. 3). As the flame is

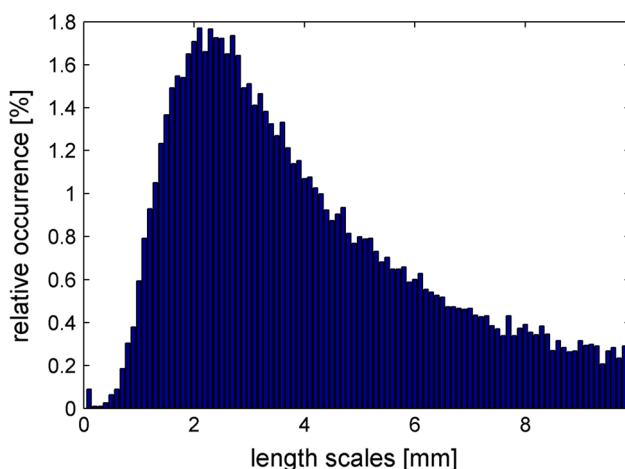


Fig. 4 Histogram of the calculated length scales along the flame front. The length scale is defined as the diameter of a *circle* with equivalent curvature as the local curvature of the flame front. The curvatures are calculated from the 2D flame fronts evaluated in the recorded images

lit, the beam steering can be seen in the slight shift of the lines in the dye cell positioned after the flame. The laser sheet furthest away from the center of the burner is located outside the flame front and only propagates through the burnt region. Here, the beam steering is small, and a standard deviation of the line positions in the image of the dye cell of 0.13 pixels, or 6 μm , is measured. In the center of the flame, where the flame front intersects the laser sheet, the beam steering increases the standard deviation in the line position to 64 μm . The maximum measured shift in a line position, recorded when the line in the sheet intersects perpendicular to the flame tip, is 204 μm (4.5 pixels in the image of the dye cell). The dye cell is positioned 20 cm from the burner. Assuming that the beam steering is induced in the entry side of the flame, this would imply a maximum beam steering inside the flame of 20 μm , which is small in relation to the acquired spatial resolution.

In summary, a spatial and temporal resolution of $3.2 \times 3.2 \times 0.75$ lines/mm and 2 ms, respectively, are obtained in a measurement volume spanning $11 \times 22 \times 6$ mm during a time span of 0.5 s. In comparison, the uncertainties due to beam steering and in predicted sheet position are negligible.

4 OH concentration

Several approaches have been pursued in the past to calculate the OH concentration from recorded LIF data. By exciting the molecule in the saturated regime and calibrating the response against a known source, as in Chen and Bilger (2001), the result becomes independent of quenching. However, this requires a top-hat laser energy profile, both in time, space and frequency, which is difficult to achieve in practice. Also, it requires higher laser fluence than what is available with the current laser system. In the linear regime, one option is to illuminate the flame with two counter-propagating laser sheets. This approach also provides quenching-independent concentration data. However, it is based on the derivative of the measured quantities (Versluis et al. 1997). It is thus noise sensitive and may not be suitable for single-shot measurements. Here, a similar approach to what is outlined in Hertz and Alden (1987) and utilized in Arnold et al. (1997) is applied. The integrated absorption is measured and related to the integrated fluorescence. This information is thereafter used to deduce the local absorption and irradiance from the local fluorescence signal. Instead of applying the iterative manner, as proposed in Hertz and Alden (1987), a more direct approach, similar to what is described in Wellander et al. (2011), is here applied. In this session, the approach is first described, together with a discussion regarding major error sources before the result is presented.

4.1 Absorption coefficient

In the linear regime, the recorded OH signal, S_f , can be written as

$$S_f = \Phi N \sigma_0 Q_f \varepsilon \quad (4)$$

where Φ represents the fluence, and N is the number density of OH present in the targeted ground state. In our case, the rotational state with $J = 7.5$ is chosen due to its weak dependency on temperature. By calculating the rotational population distribution in the interval of 1,300–2,000 K (Eckbreth 1996), one finds that the fraction of OH radicals present in this state changes by <5 %. σ_0 is the effective peak absorption cross-section, Q_f is the fluorescence quantum yield, and ε is the camera function, including solid angle of detection, objective transmittance, gain in the image intensifier and quantum efficiency and fill factor of the camera. As the light propagates through the sample, it gets attenuated due to the absorption. The decrease in Φ can be described by the Beer–Lambert law

$$\Phi(x + dx) = \Phi(x)e^{-N\sigma_0 dx} = \Phi(x)e^{-\alpha' dx} \quad (5)$$

where dx is the distance corresponding to the pixel size divided by the optical magnification, and $\alpha' = N\sigma_0$ is the absorption coefficient. Assuming that the quenching is constant throughout the flame, the sum of all recorded signal can be related to the amount of absorbed light as

$$\sum_{w,h} S_f = Q_f \varepsilon \sum_h (\Phi_0 - \Phi_f) \quad (6)$$

where Φ_0 and Φ_f stand for the initial and final fluence, respectively. Equation (6) provides a measure of the camera function times the fluorescence quantum yield which can be inserted in Eq. (4) to give a function of the absorption coefficient

$$\alpha' = N\sigma_0 = \frac{S_f \sum_h \Phi_0 - \Phi_f}{\Phi \sum_{w,h} S_f} \quad (7)$$

If different quenching rates can be expected for different heights in the burner the camera function, as given in Eq. (6) could be expressed as a function of height over the burner. However, in the present case, there is no reason to expect the quenching rate to change more as a function of height than across the flame. Also, the temperature gradients over the flame fronts introduce beam steering that slightly shifts the position of the laser light at the second dye cell. Thus, an error is induced in the height of the measured absorption that would introduce artificial lines in the calculated absorption coefficient around the flame fronts. For these reasons, the absorption and fluorescence

are integrated over the height of the laser sheet prior the calculation of the camera function.

Before any OH radical has been excited, the fluence will be proportional to the signal recorded from the first dye cell. Thus, in the first column of pixels that contain any signal (from the side where the laser sheet enters), Eq. (7) can be used directly to calculate the absorption coefficient. Equation (5) can thereafter be used to calculate the fluence level in the next column of pixels which, used in Eq. (7), provide the absorption coefficient here. This procedure is repeated until the absorption coefficient and fluence level are calculated in the entire measurement volume. In contrast to the work of Wellander et al. (2011), the attenuation of the fluorescence light in between the measurement plane and the camera has here been neglected. The reason for this is twofold. First, the spectral shape of the fluorescence light is different from the laser light. Thus, the absorption cross-section is different and has a stronger temperature dependency. Secondly, the entire volume is not recorded instantaneously, and the OH concentration may change during the scan. A method to compensate for this non-instantaneous recording in terms of the calculated flame front position is presented later in the paper. However, compensation of the OH concentration distribution is not as straight forward. The absorption of the laser light through the entire flame is about 30 %. Considering that the absorption cross-section of the $Q_1(7)$ line is relatively high in comparison with the other transitions and that only half the flame is probed, the reabsorption of the emitted light should be less than 15 %. Since the camera function is calculated from the ratio between the fluorescence signal and the absorption in the flame, the average reabsorption is already compensated for in the calculations and it is only the relative difference in absorption of the signal that induces an error.

4.2 OH concentration

From the spectral shape of the probed absorption line and knowledge of the oscillator strength, the effective absorption cross-section can be calculated (see appendix in Versluis et al. (1997) for a thorough description). In short, the integrated absorption cross-section is related to the oscillator strength, which can be calculated based on numbers found in the literature (Dieke and Crosswhite 1962; Learner 1962; Luque and Crosley 1998). The effective peak absorption cross-section, σ_0 , is effected both by collisional and Doppler line broadening and by the spectral width of the exciting laser light. An excitation scan includes all these effects, and the effective peak absorption cross-section can be calculated from the ratio between the peak and the integrated absorption cross-section of the line. Since one side of the probed $Q_1(7)$ line partly overlaps the

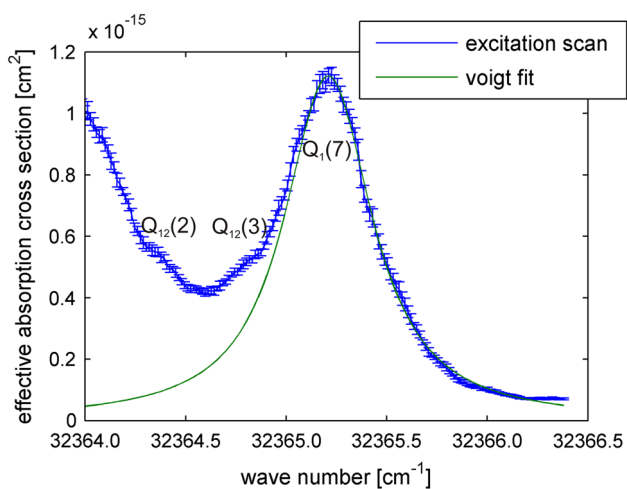


Fig. 5 Excitation scan over the $Q_1(7)$ and neighboring lines. The Voigt function is fitted to the data points on the right side of the peak where the data are not influenced by the $Q_{12}(3)$ line

$Q_{12}(3)$ line (see Fig. 5), the integration is performed on a Voigt function fitted to the unaffected part of the curve (half the peak). With the current experimental conditions, the effective peak absorption cross-section for the $Q_1(7)$ line is calculated to $\sigma_0 = 1.12 \times 10^{-15} \text{ cm}^2$. With this information, the number density of the OH radicals can be calculated from the relationship $N_{\text{tot}} = (\alpha'/\sigma_0)/(N_{J=7.5}/N_{\text{tot}})$, where $(N_{J=7.5}/N_{\text{tot}}) = 9.23 \%$ is the fraction of molecules in the $J = 7.5$ rotational state calculated at 1,750 K. The temperature in the calculation is estimated from the best fit of the absorption spectra simulated in LIFBASE (Luque and Crosley 1999) at different temperatures to the measured absorption spectra.

4.3 Error sources

In addition to the temperature influence in the ground-state population and the reabsorption of the fluorescence, as already discussed, there are several error sources affecting the accuracy in the calculation of the OH concentration. First of all, the assumption of a homogeneous quenching rate is not valid everywhere in the flame. In fact, the quenching rate varies with both temperature and surrounding composition. Assuming a constant quenching rate will yield an under prediction of the OH concentration in the reaction zone where the variations in temperature and the concentration of surrounding molecules are large. However, in the end gas zone, the results can be considered valid, since the quenching rate here is close to constant (Jonsson et al. 2013). One could argue that since the calculated absorption coefficient depends on the ratio between the total absorption and total fluorescence signal, an under

prediction of the absorption coefficient in the reaction zone will appear as an over prediction of the absorption coefficient in the product zone. However, since the thickness of the reaction zone is thin in relation to the product zone, this impact is small.

An error in the estimated line width in the excitation scan of 10 % would introduce an error in the estimated effective absorption coefficient of 9 %. Any temperature variation in the flame changes the Doppler width of the line shape and thereby induces a shift in the effective absorption cross-section. From simulations in LIFBASE (Luque and Crosley 1999), a variation of the temperature in the interval 1,500–2,500 K would correspond to a variation in the peak absorption cross-section of 15 %.

Saturation effects in the image intensifier MCP, as reported in (Weber et al. 2011), are estimated to be within 5 %. The error is estimated by measuring on a constant light source corresponding to the same signal level as in the recording of the flame. The reason the error is small despite the high frame rate is partly because the camera is more sensitive than the cameras used in Weber et al. (2011) and the signal level is kept low (~ 400 out of 4,000 counts).

4.4 Results

Figure 6 shows a comparison between OH fluorescence recorded in the center of the flame and the OH concentration calculated from the same data. In both images, the data have been filtered with a Gaussian low-pass filter (as described in Sect. 3) to suppress the high-frequency noise generated in the image intensifier. The filtering is done before the calculation of the OH concentration. Note that in the quantification process of the data in terms of OH concentration distribution, the artifacts created by the spatial profile of the laser sheet and the laser attenuation have been removed. Figure 7 shows iso-surfaces where the number density of OH equals $1.5 \times 10^{15} \text{ molecules cm}^{-3}$, corresponding to approximately one-third of the value in the flame front. Thus, the inner surface represents a surface close to the flame front, and the outer surface represents the position where two-thirds of the OH concentration has been consumed. Here, the time evolution of the flame front position can be clearly followed, indicating that the time resolution is sufficient for the present flame. During the ~ 4 -ms duration of the time series, a smooth undulating motion of the flame front can be noted. A longer sequence of the same recording can be seen in the attached movie (Online Resource 1). Since the gradient is small in the burnt gas region, the position of the outer iso-surface is flickering in between images.

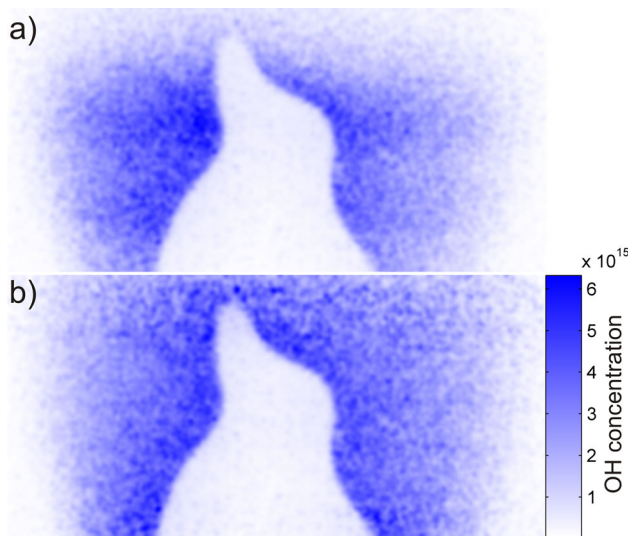


Fig. 6 Comparison between the **a** uncorrected but filtered signal and **b** calculated OH number density (molecules/cm³)

5 Flame front detection

The gradient in the OH fluorescence signal has proven to be a good marker of the flame front in premixed turbulent combustion (Hartung et al. 2008). Here, this approach is utilized with focus on the challenges associated with the third spatial dimension. Also, the non-instantaneous nature of the recording is compensated for by linearly interpolate the calculated flame front positions to a common time.

5.1 Flame front determination

The flame front is determined from the steepest gradient in each image where after it is interpolated between the measured planes into a 3D surface. Since the gradient of the signal level is independent on the absolute signal level, a calculation of the OH concentration before the gradient is calculated would only have a minor effect on the estimated flame front position. Therefore, the signal is only

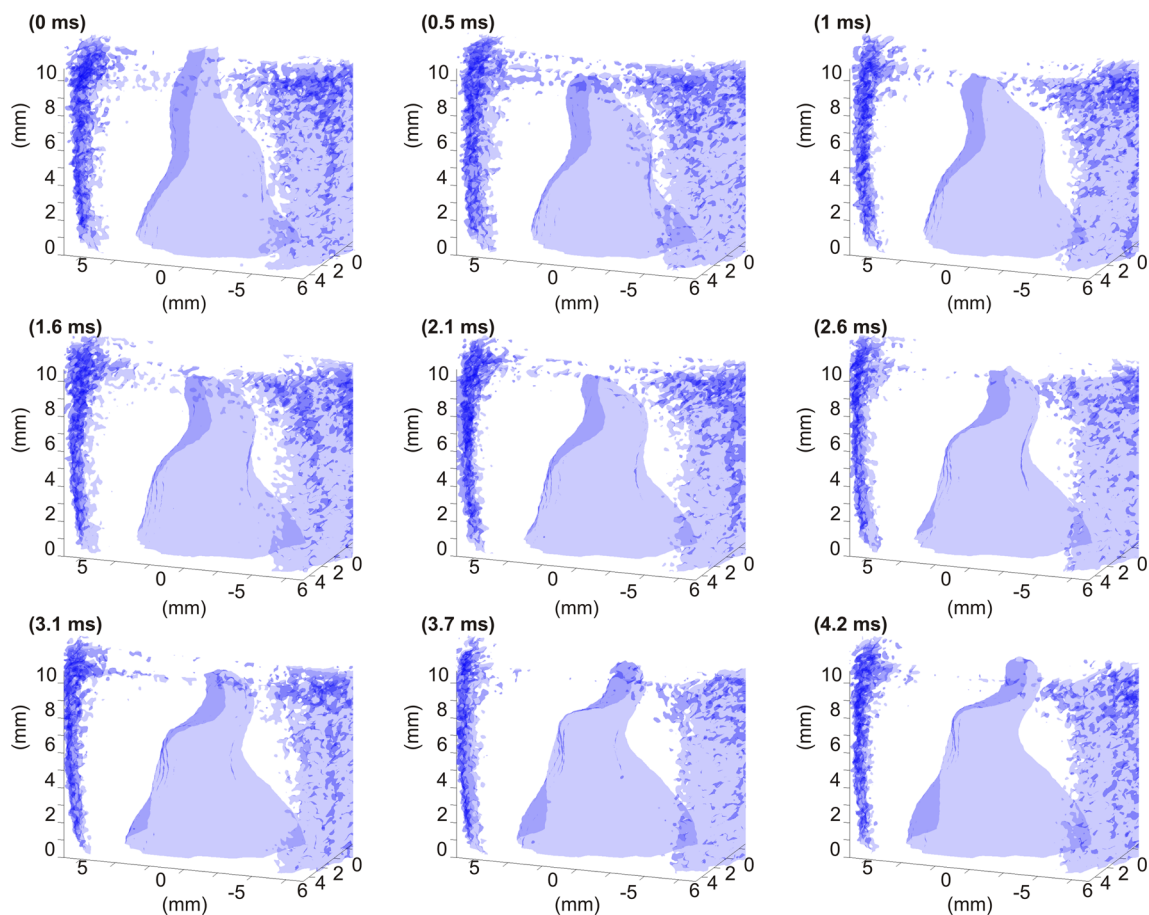


Fig. 7 Isosurfaces connecting the regions with an OH number density of $1.5 \times 10^{15} \text{ cm}^{-3}$, corresponding to approximately one-third of the concentration in the flame front. Nine images from a sequence of 1,000 3D images recorded at $\sim 2 \text{ kHz}$ are shown. Each

iso-surface is based on 10 2D OH concentration maps recorded during one scan. The scanning spans half the flame. Online Resource 1 shows a longer sequence of the same recording

compensated for the inhomogeneity in the spatial energy profile of the laser sheets. The images are also filtered with a Gaussian low-pass filter, as described in Sect. 3, to suppress the high-frequency noise generated in the image intensifier. To further improve the robustness of the edge detection, 100 iterations of a nonlinear diffusion filter with additive operator splitting, is applied to each image (Weickert et al. 1998). Here, the diffusion equation is defined as

$$d(g) = 1 - e^{-(g/1.1052)^{-2}}, \quad g > 0$$

$$d(g) = 1, \quad g \leq 0 \quad (8)$$

where g represents the gradient in the image after convolution with a Gaussian with standard deviation 1 pixel.

The flame front position is thereafter calculated from the steepest gradients of the filtered signal using the Canny edge detection scheme (Canny 1986), but with fixed thresholds. In the original version of the Canny edge detection scheme, the thresholds are set as a fraction of the maximum gradient in the current image. Here, the thresholds are set to an absolute value to ensure that all images are treated equally. For a single image, thresholds can easily be selected that explicitly detects the flame front, even without prior nonlinear diffusion filtering. However, in a data set of thousands of images, the task to find one set of filtering and threshold parameters that can distinguish all the flame fronts from the background noise become more demanding. To overcome this problem, the Canny edge thresholds are set low, so that all flame fronts are detected, but without excluding all gradient in the end gas zone. The gradients that do not belong to the flame fronts are subsequently removed using a set of selection rules. For a gradient to be accepted as a flame front, it has to

- have a positive gradient in the direction from the unburnt to the burnt gas region.
- either
 - be connected to the bottom of the image with both endpoints (anchored to the burner),
 - have endpoints connected to each other (detached or bridged flame front),
 - have both endpoints connected to the upper part of the image (considered a detached or bridged flame front propagating out of the image),
 - or have only one endpoint anchored to the burner. In this case, there must also exist a second valid segment with only one endpoint connected to the burner (considered a broken flame front or one exceeding above the imaged area).
- circumscribe an area that partly overlap the circumscribed area from the valid flame fronts in the data

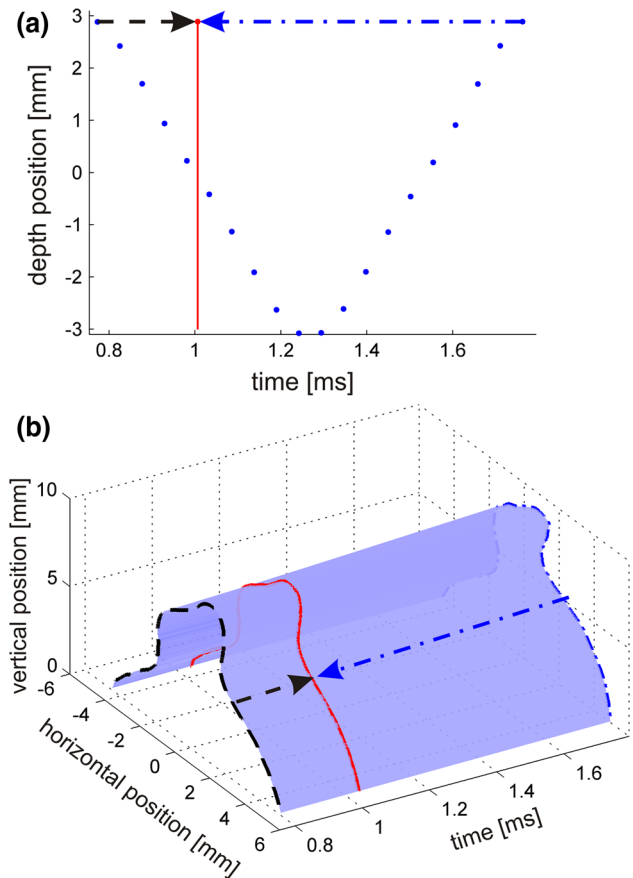


Fig. 8 Time interpolation of the calculated flame front. **a** Depth positions of the laser sheet at different timings. The *solid line* corresponds to the central scan position, i.e., the time position to where the flame fronts during one scan is interpolated. **b** Two flame fronts from the same depth position but recorded at different times are plotted with a surface linearly interpolated in between. The flame position at the central time position of the scan is calculated from the interpolation and indicated by a *solid line*

recorded at one of the adjacent depth positions (the unburnt region must cover more than one plane).

5.2 Compensation for the non-instantaneous recording of each 3D image

Ideally, all ten 2D images used to reconstruct one 3D flame front should be recorded simultaneously, or at least during a time interval smaller than the time it takes for the flame front to translate a resolvable distance. In the presented experimental approach, the time separation between the 2D images is constant. Thus, with a given sampling rate, for which a displacement of the flame front between two 3D images can be detected, the flame has also moved during the recording of one 3D image, inducing an artificial skew to the final result. Here, the outer part of the recorded volume, corresponding to the turning points of the scan, is

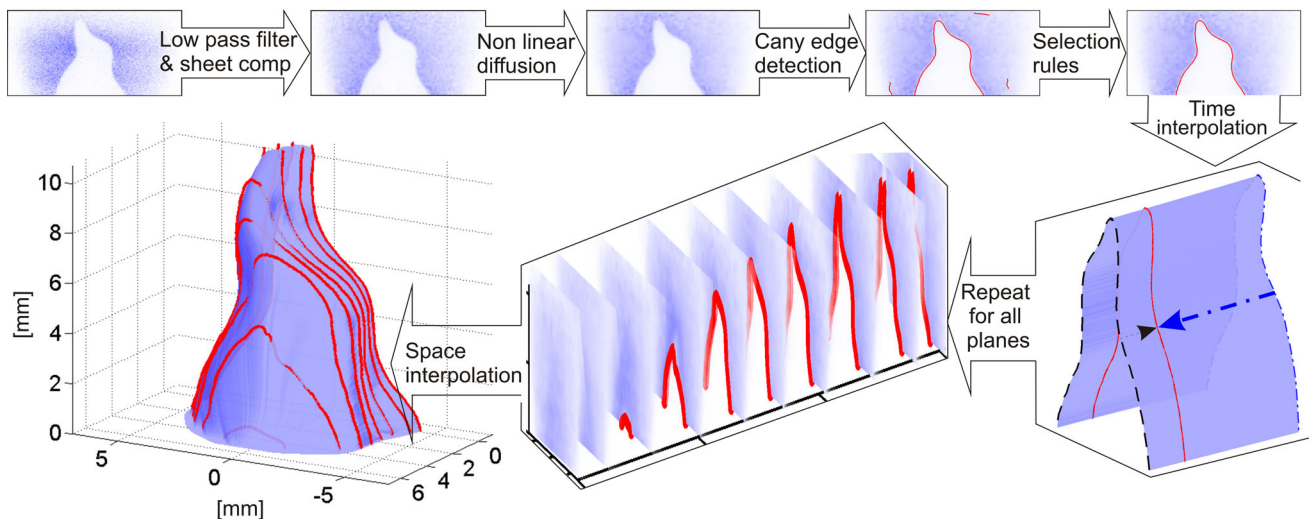


Fig. 9 Illustration of the calculation of the flame front with intermediate results shown. The raw images are low-pass filtered and divided with the spatial energy profile of the laser sheet. A nonlinear diffusion filter is applied, and Canny edge detection is used

to detect the flame fronts. False flame fronts are removed, and the flame front positions are interpolated to the time corresponding to the center of the scan. A 3D flame front surface is finally fitted to the 2D flame fronts

recorded with a time difference alternating between 1 ms and 50 μ s (see Fig. 2). Thus, if the recording of one 3D image is considered instantaneous, the flame would seem to alternate velocity from frame to frame in these parts of the volume. To remove this artifact, the flame front position during one scan is linearly interpolated to a common time position of the scan, as shown in Fig. 8. In order to minimize the longest interpolation time step, the time for the center position of the scan is chosen as target for the interpolation.

5.3 Three-dimensional surface

When the flame fronts have been detected, separated from the artefacts and interpolated to the common time positions, surfaces are fitted to each set of ten consecutive 2D flame fronts recorded from each scan, using a second-order non-uniform rational B-splines (NURBS) interpolation (Piegl 1991). The steps in the image processing are illustrated in Fig. 9.

Figure 10 shows a sequence of nine out of 1,000 images in one recording. Note the similarity with the inner iso-surface of the OH concentration presented in Fig. 7. A longer portion of the recording is attached in a movie format (Online Resource 2).

6 Discussion

A measurement technique capable of recording three-dimensional time-resolved data of the OH radical has been

presented. Measurements and calculations of the OH concentration and the flame front have been demonstrated. The artifacts in the flame front introduced by the non-instantaneous recording of each 3D image have been compensated for by linearly interpolating the flame front positions to a common time. Higher-order interpolation could be considered to increase the precision in the final result. A similar interpolation for the OH concentration could also be done if the flow field were measured simultaneously.

Spatial and temporal resolution of $3.2 \times 3.2 \times 0.75$ lines/mm and 2 ms, respectively, are obtained in a measurement volume spanning $11 \times 22 \times 6$ mm during a time span of 0.5 s. The spatial and temporal resolution and the recorded volume are linked to each other. For the visual impression, the amplitude is here adjusted to cover half the flame. As a consequence, some of the length scales remain unresolved. In an experiment focusing on the flame properties, a smaller amplitude should be selected. This would not only increase the depth resolution, but also reduce the required depth of field and thereby enabling more light to be collected. As a consequence, the need for filtering is reduced, increasing the in-plane spatial resolution.

The beam steering has been measured and shown to be insignificant within the flame. For the measured absorption, on the other hand, it is not negligible. A solution to this problem could be to image the flame on the dye cells in a 4f setup as done in Arnold et al. (1997).

With the rapid development of higher-repetition-rate lasers, both in terms of diode-pumped pulsed laser operated continuously as applied in this paper, and burst mode lasers (Thurrow et al. 2013), the presented technique holds

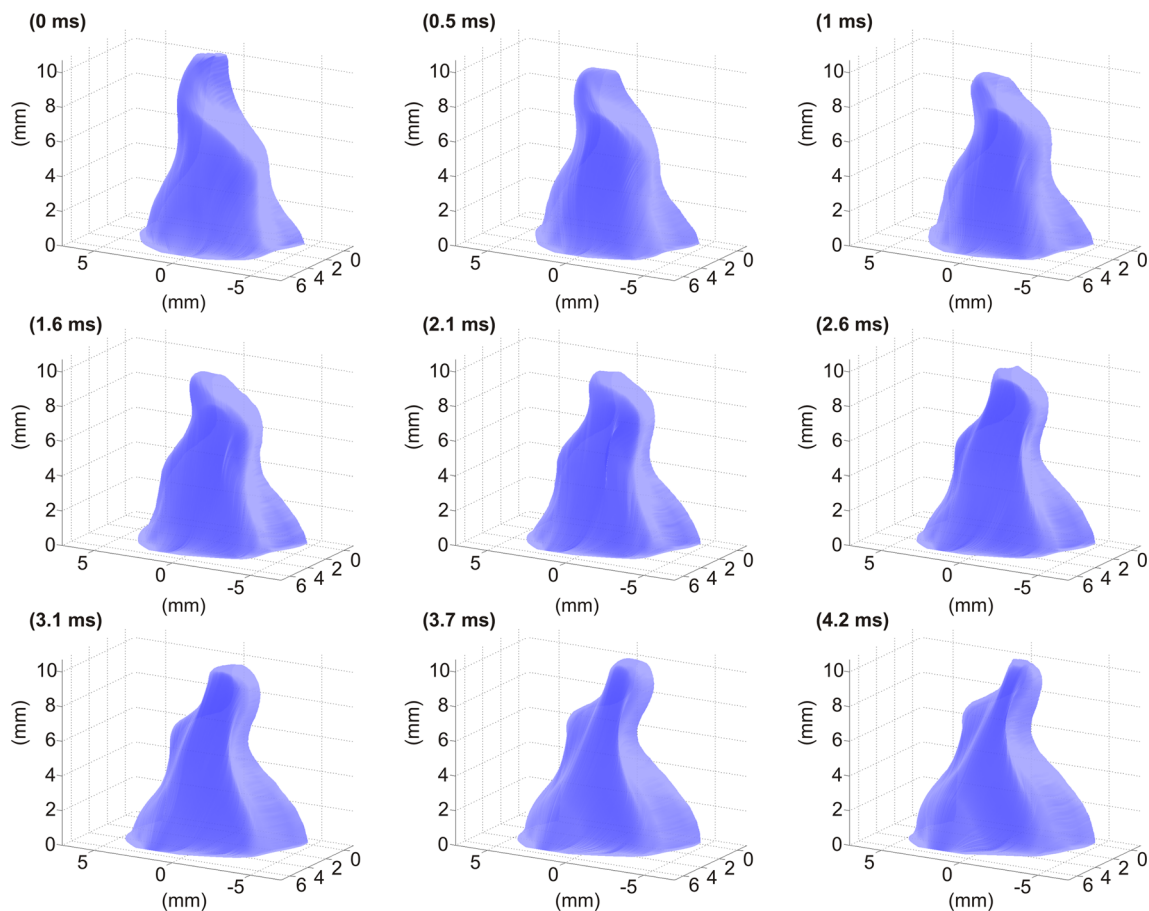


Fig. 10 Nine images from a sequence of 1,000 3D images recorded at ~ 2 kHz are shown. The semi-transparent surfaces are calculated from the 2D flame fronts using NURBS interpolation. Each 3D image consists of 10 2D flame fronts recorded during one scan and linearly

interpolated to the center time point of the scan. The scanning spans half the flame. Online Resource 2 shows a longer sequence of the same recording

considerable promise for measurements also in more turbulent reacting flows, where better time resolution is required.

Acknowledgments The authors wish to thank the ERC Advanced grant DALDECS and the Swedish Energy Agency for financial support.

References

- Arnold A, Bombach R, Kappeli B, Schlegel A (1997) Quantitative measurements of OH concentration fields by two-dimensional laser-induced fluorescence. *Appl Phys B* 64(5):579–583. doi:10.1007/s003400050218
- Cai WW, Li XS, Li F, Ma L (2013) Numerical and experimental validation of a three-dimensional combustion diagnostic based on tomographic chemiluminescence. *Opt Express* 21(6):7050–7064
- Canny J (1986) A computational approach to edge-detection. *IEEE Trans Pattern Anal Mach Intell* 8(6):679–698
- Chen Y-C, Bilger RW (2001) Simultaneous 2-D imaging measurements of reaction progress variable and OH radical concentration in turbulent premixed flames: experimental methods and flame brush structure. *Combust Sci Technol* 167(1):131–167. doi:10.1080/00102200108952180
- Dieke GH, Crosswhite HM (1962) The ultraviolet bands of OH fundamental data. *J Quant Spectrosc Radiat Transfer* 2(2):97–199. doi:10.1016/0022-4073(62)90061-4
- Dyer MJ, Crosley DR (1982) Two-dimensional imaging of OH laser-induced fluorescence in a flame. *Opt Lett* 7(8):382–384. doi:10.1364/ol.7.000382
- Eckbreth AC (1996) *Laser diagnostics for combustion temperature and species*, vol 3. CRC Press, Taylor & Francis, London
- Hartung G, Hult J, Kaminski CF, Rogerson JW, Swaminathan N (2008) Effect of heat release on turbulence and scalar-turbulence interaction in premixed combustion. *Phys Fluids* (1994-present) 20(3). doi:10.1063/1.2896285
- Hertz HM, Alden M (1987) Calibration of imaging laser-induced fluorescence measurements in highly absorbing flames. *Appl Phys B* 42(2):97–102. doi:10.1007/bf00694817
- Hult J, Omrane A, Nygren J, Kaminski CF, Axelsson B, Collin R, Bengtsson PE, Alden M (2002) Quantitative three-dimensional imaging of soot volume fraction in turbulent non-premixed flames. *Exp Fluids* 33(2):265–269. doi:10.1007/s00348-002-0410-2
- Jonsson M, Ehn A, Christensen M, Aldén M, Bood J (2013) Simultaneous one-dimensional fluorescence lifetime measurements

- of OH and CO in premixed flames. *Appl Phys B* 1–9. doi:[10.1007/s00340-013-5570-7](https://doi.org/10.1007/s00340-013-5570-7)
- Kaminski CF, Hult J, Alden M (1999) High repetition rate planar laser induced fluorescence of OH in a turbulent non-premixed flame. *Appl Phys B* 68(4):757–760. doi:[10.1007/s003400050700](https://doi.org/10.1007/s003400050700)
- Karpets AN, Settersten TB, Schefer RW, Barlow RS (2004) Laser imaging system for determination of three-dimensional scalar gradients in turbulent flames. *Opt Lett* 29(4):355–357. doi:[10.1364/ol.29.000355](https://doi.org/10.1364/ol.29.000355)
- Kychakoff G, Paul PH, Vancruyningen I, Hanson RK (1987) Movies and 3-D images of flowfields using planar laser-induced fluorescence. *Appl Opt* 26(13):2498–2500
- Learner RCM (1962) The influence of vibration-rotation interaction on intensities in the electronic spectra of diatomic molecules. I. The hydroxyl radical. *Proc R Soc Lond A Math Phys Sci* 269(1338):311–326. doi:[10.1098/rspa.1962.0179](https://doi.org/10.1098/rspa.1962.0179)
- Luque J, Crosley DR (1998) Transition probabilities in the $A\ 2\Sigma + - X\ 2\Pi$ electronic system of OH. *J Chem Phys* 109(2):439–448. doi:[10.1063/1.476582](https://doi.org/10.1063/1.476582)
- Luque J, Crosley DR (1999) LIFBASE: Database and spectral simulation program (version 1.5) SRI international report MP 99-009
- Nygren J, Hult J, Richter M, Alden M, Christensen M, Hultqvist A, Johansson B (2002) Three-dimensional laser induced fluorescence of fuel distributions in an HCCI engine. *Proc Combust Inst* 29:679–685. doi:[10.1016/s1540-7489\(02\)80087-6](https://doi.org/10.1016/s1540-7489(02)80087-6)
- Olofsson J, Richter M, Alden M, Auge M (2006) Development of high temporally and spatially (three-dimensional) resolved formaldehyde measurements in combustion environments. *Rev Sci Instrum* 77(1). doi:[10.1063/1.2165569](https://doi.org/10.1063/1.2165569)
- Oyoung F, Bilger RW (1997) Scalar gradient and related quantities in turbulent premixed flames. *Combust Flame* 109(4):682–700. doi:[10.1016/s0010-2180\(97\)00056-4](https://doi.org/10.1016/s0010-2180(97)00056-4)
- Piegl L (1991) On NURBS: a survey. *IEEE Comput Graph Appl* 11(1):55–71. doi:[10.1109/38.67702](https://doi.org/10.1109/38.67702)
- Shannon CE (1949) Communication in the presence of noise. *Proc Inst Radio Eng* 37(1):10–21. doi:[10.1109/jrproc.1949.232969](https://doi.org/10.1109/jrproc.1949.232969)
- Smith JD, Sick V (2005) Crank-angle resolved imaging of biacetyl laser-induced fluorescence in an optical internal combustion engine. *Appl Phys B* 81(5):579–584. doi:[10.1007/s00340-005-1947-6](https://doi.org/10.1007/s00340-005-1947-6)
- Steinberg AM, Boxx I, Arndt CM, Frank JH, Meier W (2011) Experimental study of flame-hole reignition mechanisms in a turbulent non-premixed jet flame using sustained multi-kHz PIV and crossed-plane OH PLIF. *Proc Combust Inst* 33:1663–1672. doi:[10.1016/j.proci.2010.06.134](https://doi.org/10.1016/j.proci.2010.06.134)
- Thurrow BS, Lynch KP (2009) Development of a high-speed three-dimensional flow visualization technique. *AIAA J* 47(12):2857–2865. doi:[10.2514/1.41788](https://doi.org/10.2514/1.41788)
- Thurrow B, Jiang NB, Lempert W (2013) Review of ultra-high repetition rate laser diagnostics for fluid dynamic measurements. *Meas Sci Technol* 24(1). doi:[10.1088/0957-0233/24/1/012002](https://doi.org/10.1088/0957-0233/24/1/012002)
- Trunk PJ, Boxx I, Heeger C, Meier W, Boehm B, Dreizler A (2013) Premixed flame propagation in turbulent flow by means of stereoscopic PIV and dual-plane OH-PLIF at sustained kHz repetition rates. *Proc Combust Inst* 34:3565–3572. doi:[10.1016/j.proci.2012.06.025](https://doi.org/10.1016/j.proci.2012.06.025)
- Versluis M, Georgiev N, Martinsson L, Alden M, Kroll S (1997) 2-D absolute OH concentration profiles in atmospheric flames using planar LIF in a bi-directional laser beam configuration. *Appl Phys B* 65(3):411–417. doi:[10.1007/s003400050289](https://doi.org/10.1007/s003400050289)
- Weber V, Brubach J, Gordon RL, Dreizler A (2011) Pixel-based characterisation of CMOS high-speed camera systems. *Appl Phys B* 103(2):421–433. doi:[10.1007/s00340-011-4443-1](https://doi.org/10.1007/s00340-011-4443-1)
- Weickert J, Romeny BMTH, Viergever MA (1998) Efficient and reliable schemes for nonlinear diffusion filtering. *IEEE Trans Image Process* 7(3):398–410. doi:[10.1109/83.661190](https://doi.org/10.1109/83.661190)
- Wellander R, Berrocal E, Kristensson E, Richter M, Alden M (2011) Three-dimensional measurement of the local extinction coefficient in a dense spray. *Meas Sci Technol* 22(12). doi:[10.1088/0957-0233/22/12/125303](https://doi.org/10.1088/0957-0233/22/12/125303)
- Winter M, Lam JK, Long MB (1987) Techniques for high-speed digital imaging of gas concentrations in turbulent flows. *Exp Fluids* 5(3):177–183
- Yip B, Lam JK, Winter M, Long MB (1987) Time-resolved three-dimensional concentration measurements in a gas jet. *Science (New York, NY)* 235(4793):1209–1211. doi:[10.1126/science.235.4793.1209](https://doi.org/10.1126/science.235.4793.1209)
- Yip B, Schmitt RL, Long MB (1988) Instantaneous three-dimensional concentration measurements in turbulent jets and flames. *Opt Lett* 13(2):96–98. doi:[10.1364/OL.13.000096](https://doi.org/10.1364/OL.13.000096)